Contrast Behavior and Relaxation Effects of Conventional and Hyperecho-Turbo Spin Echo Sequences at 1.5 and 3 T[1]

Matthias Weigel* and Juergen Hennig

To overcome specific absorption rate (SAR) limitations of spin-echo-based MR imaging techniques, especially at (ultra) high fields, rapid acquisition relaxation enhancement/TSE (turbo spin echo)/fast spin echo sequences in combination with constant or variable low flip angles such as hyperechoes and TRAPS (hyperTSE) have been introduced. Due to the multiple spin echo and stimulated echo pathways involved in the signal formation, the contrast behavior of such sequences depends on both T_2 and T_1 relaxation times. In this work, constant and various variable flip angle sequences were analyzed in a volunteer study. It is demonstrated that a single effective echo time parameter TE_{eff} can be calculated that accurately describes the overall T_2 weighted image contrast. TE_{eff} can be determined by means of the extended phase graph concept and is practically independent of field strength. Using the described formalism, the contrast of any TSE sequence can be predicted. HyperTSE sequences are demonstrated to show a robust and well-defined T_2 contrast allowing clinical routine MRI to be performed with SAR reductions of typically at least 70%.   Magn Reson Med 55: 826–835, 2006. © 2006 Wiley-Liss, Inc.

Key words: TSE; T_2; T_1; variable flip angles; hyperecho; TRAPS

Multi spin-echo sequences such as rapid acquisition relaxation enhancement [turbo spin echo (TSE), fast spin echo. . .)] (1) find widespread applications in clinical routine MRI examinations. Insensitivity to susceptibility and field inhomogeneity effects, well-defined contrast behavior (e.g., a pure T_2 contrast), and sensitivity to a variety of pathologic conditions have made such techniques an indispensable tool for clinical diagnosis.

With increasing field strength the pronounced RF power deposition (RFP) caused by the multiple refocusing pulses is becoming increasingly problematic. The specific absorption rate (SAR) problem is further emphasized by the use of fast gradients leading to short echo spacings (ESP) as needed in applications such as multislice T_2 weighted imaging of the abdomen in a single breathhold. Different options exist to avoid the SAR limitations for patient safety: The most straightforward approaches include a reduction of the number of slices, shortening of the echo train length (ETL), an increase in TR, or the use of longer RF pulses with simpler pulse shapes (2). Consequently, dis-

advantages such as limited volume coverage, longer acquisition times, and a less well defined slice profile emerge. These limitations are not acceptable for most clinical applications. More promising solutions are a shorter ETL via partially parallel acquisition (PPA) techniques such as GRAPPA, SMASH, and SENSE (3,4) or partial Fourier reconstruction methods (5,6).

Since $SAR \sim RFP \sim \alpha_{ref^2}$ the use of refocusing flip angles lower than 180° reduces RFP very efficiently (7). However, a reduction of the (constant) refocusing flip angle leads to a diminished signal-to-noise ratio (SNR) and also to subtle changes of contrast due to stimulated echo contributions that are usually ignored.

Recently, more sophisticated RF pulse mechanisms using varying flip angles have been proposed (8–11). In general, these techniques use high flip angles to produce high signal for the encoding of central k-space and lower flip angles for the acquisition of outer parts of k-space. Such symmetrical or asymmetrical hyperechoes (TRAPS, transition into static pseudo steady state) have been shown to provide full signal intensity for the central part of k-space at considerable reduction of SAR. Typical SAR reductions are on the order of 70%. Initial clinical studies with T_2 weighted hyperecho-TSE sequences have demonstrated the clinical usefulness of this approach (12). In addition, the application of TRAPS for low SAR inversion recovery (IR) weighted TSE sequences was recently reported (13).

The original hyperecho approach (9) is based on an anti-symmetric arrangement of flip angles around a central 180° pulse in order to completely refocus magnetization during the acquisition of central phase encoding lines. TRAPS (8) has been introduced as a more general approach that allows the flip angles to be varied freely throughout the RF pulse train after a transition into the static pseudo steady state (sPSS) (14–16). TRAPS is more flexible and permits a direct shaping of the point spread function (PSF), which can be used to even improve image sharpness compared to standard TSE (17). In a slightly different approach Busse (10) suggested maintaining high flip angles of approximately 150° until the k-space center has been acquired, followed by monotonically reduced flip angles thereafter. This approach mostly maintains the pure T_2 contrast of the central k-space signal but limits the achievable SAR reduction and leads to additional image blurring. An alternative 3D-TSE sequence by Mugler et al. (11) uses very long echo trains with extremely low flip angles as small as 20°.

The aim of this work is to present the results of a volunteer study on the contrast behavior of different types of T_2 weighted TSE sequences with constant and varying flip angles. An overview of examples employing hyperTSE (TRAPS) and various combinations of TE and ETL and

their respective SAR reduction is presented. Based on the theoretical framework presented in an earlier paper (8), T_1 and T_2 contributions of the multiple signal pathways are calculated and compared to the experimental results. The results demonstrate that the intrinsic contrast of any generic TSE sequence with arbitrary flip angles can be a priori predicted employing the extended phase graph (EPG) concept (18). This concept is used to introduce specific contrast corrections for an adapted effective T_2 weighting, which can be expressed by an effective echo time TE_{eff} intrinsic to each sequence. The described adaptation can be directly implemented into the TSE sequence. Equivalence of contrast is demonstrated by a comparison of high-resolution contrast adapted hyperTSE and conventional TSE180° at identical TE_{eff}.

THEORY

The EPG concept allows the mixing of different magnetization pathways to be calculated in a multi spin-echo experiment. Thus, if the relaxation times T_1 and T_2 are known it is possible to quantify signal intensities of all echoes in a TSE echo train. Assuming that the contrast of an MRI image is determined by the echoes encoded for the center of k-space and that the finite-duration RF pulses can be treated as δ functions, the signal intensity $I_{predicted}$ of the nth echo for a specific MRI sequence and tissue at a given echo time TE can be predicted as (17)

$$I_{predicted}(\alpha_i, T_1, T_2) = \beta \cdot PD \cdot f_{EPG}(\alpha_{1 \ldots n}, T_1, T_2). \quad [1]$$

f_{EPG} describes the sequence specific mixing of magnetization pathways depending on all previous refocusing flip angles $\alpha_{1 \ldots n}$. It also includes signal decay due to relaxation. PD represents the proton density and β is a scaling factor that accounts for physical parameters such as coil sensitivity, receiver gain, and FFT scale factor. β is constant for the TSE and hyperTSE sequences with identical TE and ETL used in our experiments.

Since stimulated echo pathways contribute to the measured signal, whenever any of the refocusing flip angles in a multiecho sequence deviates from 180°, both T_1 and T_2 decay must be considered. According to Eq. [1] from Ref. 8, the factor f_{EPG} can be split into two components,

$$I_{predicted}(\alpha_i, T_1, T_2) = \beta \cdot PD \cdot f_a(\alpha_n) \cdot f_m(\alpha_{1 \ldots n-1}, T_1, T_2), \quad [2]$$

where f_m represents the available magnetization as a result of spin evolution for previous refocusing flip angles. The attenuation factor f_a reflects the amount of this magnetization is read out by α_n. For a conventional TSE sequence with ideal 180° pulses f_a equals 1. The same applies for a symmetrical hyperecho experiment at the time of hyperecho formation even though α_n may differ significantly from 180°. In fact, α_n can assume any arbitrary value given that the hyperecho conditions are fulfilled for all echoes. In an asymmetric hyperecho (TRAPS) experiment magnetization is always kept close to the sPSS. During the acquisition of the center of k-space, magnetization α_n is close to 180° and therefore f_a is close to 1 as well. For TSE sequences with lower but constant flip angles only some

fraction of the available magnetization is translated into signal and $f_a < 1$. For such sequences f_a is maximized if the magnetization has been prepared into the static pseudo steady state sPSS(α) for the respective α with any of the preparation sequences described in the literature (14–16). Therefore, f_a represents the signal intensity of the corresponding sPSS(α) if relaxation effects are ignored and Eq. [2] can be rewritten as

$$I_{predicted}(\alpha_i, T_1, T_2) = \beta \cdot PD \cdot f_a(\alpha_{sPSS}) \cdot f_m(\alpha_{1 \ldots n}, T_1, T_2), \quad [3]$$

where α_{sPSS} signifies the flip angle to which the sPSS refers. Eq. [3] can also be used for TRAPS-TSE implementations for which $f_a(\alpha_{sPSS}) \approx f_a(180°) = 1$ (see above). By omitting relaxation effects, the factor $f_a(\alpha_{sPSS})$ can be calculated via the EPG as

$$f_a(\alpha_{sPSS}) = f_{EPG}(\alpha_{1 \ldots n}, T_1 = T_2 = \infty). \quad [4]$$

The term f_m can be decomposed into T_1 and T_2 contributions (8)

$$f_m = \exp\left(-\frac{f_t \cdot TE}{T_2}\right) \cdot \exp\left(-\frac{(1 - f_t) \cdot TE}{T_1}\right), \quad [5]$$

where f_t represents the fraction of time during which magnetization has been present as transverse magnetization. This decomposition leads to

$$I(TE) = \beta \cdot PD \cdot f_a(\alpha_{sPSS}) \cdot \exp\left(-\frac{f_t \cdot TE}{T_2}\right) \cdot \exp\left(-\frac{(1 - f_t) \cdot TE}{T_1}\right). \quad [6]$$

From Eqs. [1] and [6] f_t is determined as

$$f_t = \frac{\ln\left(\dfrac{f_{EPG}(\cdots)}{f_a(\alpha_{sPSS})}\right) \cdot \dfrac{1}{TE} + \dfrac{1}{T_1}}{\dfrac{1}{T_1} - \dfrac{1}{T_2}} \quad [7]$$

For many biologic tissues with $T_1 \gg T_2$ and for $TE \ll T_1$ the T_1 dependent term can be neglected and (6) becomes

$$I(TE) = \beta \cdot PD \cdot f_a(\alpha_{sPSS}) \cdot \exp\left(-\frac{f_t \cdot TE}{T_2}\right). \quad [8]$$

It has already been demonstrated by numerical simulations that f_t is mostly independent of T_1 and T_2 for a broad range of relaxation times (8). It is thus reasonable to use a single characteristic value for f_t to characterize the T_2 contrast of a given TSE sequence that is identical to that of a fully refocused experiment with

$$TE_{corrected} = TE_{eff} = f_t \cdot TE. \quad [9]$$

Since $f_t < 1$ the effective echo time TE_{eff} for signal readout of central k-space data are prolonged by a factor $1/f_t$ compared to a conventional TSE sequence for equivalent T_2 contrast.

For practical applications the weak dependence of f_t on T_1 and T_2 can be employed to estimate f_t for a given TSE sequence. By defining a "virtual tissue" with arbitrary T_2 within the physiologic range (typically $T_{2\text{const}} = 100$ ms, $T_1 = \infty$) a reliable estimate for f_t can be determined as

$$f_{t\text{estimation}} = -T_{2\text{const}} \cdot \ln\left(\frac{f_{\text{EPG}}(\alpha_i, T_{2\text{const}})}{f_a(\alpha_{\text{sPSS}})}\right), \quad [10]$$

which will be shown in subsequent sections. As a result of the weak dependence of f_t on T_2, f_t and therefore TE_{eff} depend only on the sequence parameters and can therefore be calculated and displayed during sequence setup. For further automation, the user interface is modified such that f_t is calculated for any desired TE_{eff} and the proper phase encoding scheme to yield the desired T_2 contrast is automatically generated while yielding a specific reduction in SAR.

METHODS

Experiments were performed on two whole-body imaging systems at 1.5 T (Magnetom Sonata, Siemens, Erlangen, Germany, $n = 10$) and 3 T (Magnetom Trio, Siemens, $n = 13$). Sixteen cooperative healthy volunteers (between 26 and 38 years old, 14 males and 2 females) without any history of brain disease were included in the study. Seven volunteers (5 males, 2 females) were examined at both 1.5 and 3 T.

Different flip angle variation schemes were implemented into the TSE sequence provided by the manufacturer. General parameters were FOV = 24 × 20 cm², matrix = 253 × 206, BW = 210 Hz/pixel, ESP = 8.9 ms, TR = 5000 ms, sinc pulses with one sidelobe (duration = 2.56 ms). A single oblique transversal slice (slice thickness = 5 mm) in anterior–posterior cerebral commissural alignment was acquired in order to minimize magnetization transfer effects.

The following protocol was used for all experiments: First, anatomic reference scans (duration 0:54 min) were performed followed by scans to determine T_1 and T_2 relaxation times (total acquisition time 14:00 min). Subsequently, four blocks of TSE imaging sequences with two different echo times (TE = 80 ms, TE = 134 ms) and two different echo trains lengths (ETL = 15, ETL = 25) were acquired. The acquisition times for an imaging block with ETL = 15 and ETL = 25 were 13:45 and 9:10 min, respectively, leading to a total acquisition time of 60:44 min for the whole experimental protocol.

Each imaging block consisted of 11 different sequences. Five TSE measurements used constant flip angles (180, 150, 120, 90, and 60°) while different kinds of flip angle variations (ranging from 180° down to 90 or 60°) using TRAPS were applied for 6 additional scans. Linear and optimized sinusoidal flip angle ramps were employed. The acquisition parameters and the respective SAR reductions for each sequence are summarized in Table 1. A more detailed description of the TRAPS indices is given in Fig. 1 and Refs (8). and (17). Relative SAR values for generic TSE sequences compared to a TSE180° were calculated as

Table 1

Overview of Complete Imaging Part of the Protocol including Relative RF Power Deposition SAR_{rel} and Effective Echo Time TE_{eff} (identical for 1.5 and 3 T) (a) First Imaging Block with the General Parameters TE = 80 ms, ETL = 15, TR = 5000 ms

Sequence type	TRAPS Indices	SAR_{rel}/%	TE_{eff}/ ms
TSE180°	—	100	80
TSE150°	—	70	77
TSE120°	—	46	70
TSE90°	—	27	59
TSE60°	—	13	45
TRAPS90°_lin	4,9,9,15	53	70
TRAPS60°_lin	4,9,9,15	42	62
TRAPS90°_sin1	4,9,9,15	45	68
TRAPS90°_sin2	3,9,9,14	46	70
TRAPS60°_sin1	4,9,9,15	33	58
TRAPS60°_sin2	3,9,9,14	34	61

(b) Second Imaging Block with the General Parameters TE = 80 ms, ETL = 25, TR = 5000 ms

TSE180°	—	100	80
TSE150°	—	70	77
TSE120°	—	45	70
TSE90°	—	26	59
TSE60°	—	12	45
TRAPS90°_lin	4,9,9,20	48	70
TRAPS60°_lin	4,9,9,20	38	62
TRAPS90°_sin1	4,9,9,20	42	68
TRAPS90°_sin2	3,9,9,18	41	70
TRAPS60°_sin1	4,9,9,20	29	58
TRAPS60°_sin2	3,9,9,18	29	61

(c) Third Imaging Block with the General Parameters TE = 134 ms, ETL = 15, TR = 5000 ms

TSE180°	—	100	134
TSE150°	—	70	128
TSE120°	—	46	116
TSE90°	—	27	96
TSE60°	—	13	71
TRAPS90°_lin	6,15,15,16	51	114
TRAPS60°_lin	6,15,15,16	40	99
TRAPS90°_sin1	4,15,15,16	49	113
TRAPS90°_sin2	6,15,15,16	45	110
TRAPS60°_sin1	4,15,15,16	37	98
TRAPS60°_sin2	6,15,15,16	33	92

(d) Fourth Imaging Block with the General Parameters TE = 134 ms, ETL = 25, TR = 5000 ms

TSE180°	—	100	134
TSE150°	—	70	128
TSE120°	—	45	116
TSE90°	—	26	96
TSE60°	—	12	71
TRAPS90°_lin	4,15,15,25	55	118
TRAPS60°_lin	4,15,15,25	45	106
TRAPS90°_sin1	4,15,15,25	47	113
TRAPS90°_sin2	6,15,15,23	43	110
TRAPS60°_sin1	4,15,15,25	35	98
TRAPS60°_sin2	6,15,15,23	31	92

$$SAR_{\text{rel}} = \frac{1}{\text{ETL}} \cdot \sum_{i=1}^{\text{ETL}} \left(\frac{\alpha_i}{180°}\right)^2. \quad [11]$$

The relation expresses the fact that the RFP is directly proportional to the square of the refocusing flip angle.
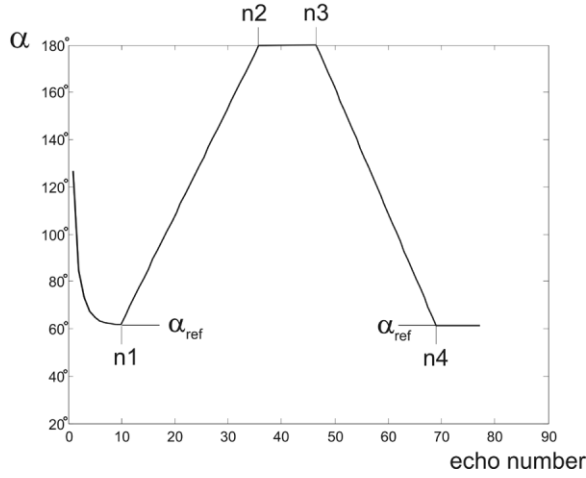
FIG. 1. Definition of TRAPS indices along the RF pulse train. An example for an echo train length of 80 is shown.

SAR_{rel} was normalized to the echo train length ETL and set to 1 for a standard TSE with ideal 180° RF pulses.

For T_1 measurements an inversion recovery prepared TSE (TE = 8.9 ms) with inversion times TI = [50, 100, 500, 1500, 3500] ms was employed. Transverse relaxation time T_2 was measured by TSE sequences with different echo times TE = [8.9, 53.4, 89.0, 222.5] ms. A repetition time of TR = 7000 ms was used for all relaxation time measurements. All other parameters were identical to those used for the TSE with flip angle variations. Pixel-by-pixel maps of relaxation times were calculated by exponential fits using the following fit functions:

$$I(TI_i) = I_0 \cdot \left(1 - a \cdot \exp\left(-\frac{TI_i}{T_1} \right) \right) \qquad [12]$$

$$I(TE_i) = I_0 \cdot \exp\left(-\frac{TE_i}{T_2} \right). \qquad [13]$$

Signal intensities I(sequence,tissue) were evaluated in global (frontal, insular, parietal, occipital) ROIs of cortical gray matter (GM) and white matter (WM), the left and right ventricle for cerebrospinal fluid (CSF), and in subcutaneous fat. Identical ROIs were used to extract the corresponding relaxation times $T_{1,tissue}$ and $T_{2,tissue}$ from the fitted maps. The average number of evaluated pixels per ROI was 450 (CSF), 630 (fat), 840 (GM), and 1360 (WM), respectively.

f_{EPG} was obtained for each measurement/sequence per tissue and volunteer by applying the measured individual values for T_1 and T_2. A common proton density value PD_{tissue} multiplied by the additional scaling factor β was assessed for all measurements for each tissue and each volunteer using the corresponding f_{EPG} and the following equation:

$$\beta \cdot PD_{tissue} = \frac{I_{measured}}{f_{EPG}(\alpha_{1\ldots n}, T_1, T_2)}. \qquad [14]$$

β*PD_{tissue} was averaged over the 11 sequences of one block for a specific TE and ETL per tissue and per volunteer to obtain β*PD_{mean} (see also Fig. 2). β*PD_{mean} was then used for the forward calculations of signal intensities via Eq. [1] for each measurement, tissue, and acquired dataset/volunteer. β*PD_{tissue} was not averaged over all 44 sequences of one dataset since β may change between sequences with different parameters TE or ETL.

Quantitative proton density ratios were obtained by dividing β*$PD_{mean,tissue}$ with β*$PD_{mean,GM}$ for each imaging block per volunteer and tissue. Hence, the scaling factor β cancels and the resulting proton density ratios were averaged over all four imaging blocks and volunteers for each tissue.

The relative deviation between the actually measured and its corresponding predicted signal intensity for each measurement/sequence, tissue, and volunteer was then computed as

$$\Delta I_{relative}(\text{sequence,tissue}) = \frac{I_{predicted} - I_{measured}}{I_{measured}}. \qquad [15]$$

Subsequently, the effective T_2 weighing factor f_t was determined from the data.

For further optional automation the employed TSE sequence was modified such that for any desired TE_{eff} the proper phase encoding scheme to yield the desired T_2 contrast is automatically generated. The implemented algorithm starts with TE = $TE_{eff-desired}$ and an initial flip angle of 60° (TRAPS60°) resulting in a maximum saving in SAR. Next, the flip angles needed for the user selected flip angle ramps are calculated. The resulting TE_{eff} is then calculated according to Eqs. [9] and [10]. Subsequently, the TE of the hyperTSE is iteratively enlarged and the corresponding flip angle ramps and TE_{eff} determined until the resulting TE_{eff} closely matches $TE_{eff-desired}$.

Finally, the feasibility of the described methods was clinically evaluated by high-resolution imaging. Five patients (between 6 and 62 years old, 4 males and 1 female) underwent MR imaging with TSE sequence used in the volunteer study (Table 1c). A higher resolution of matrix = 506 × 412 and slice thickness = 2 mm with two averages was used, while the other parameters were identical.
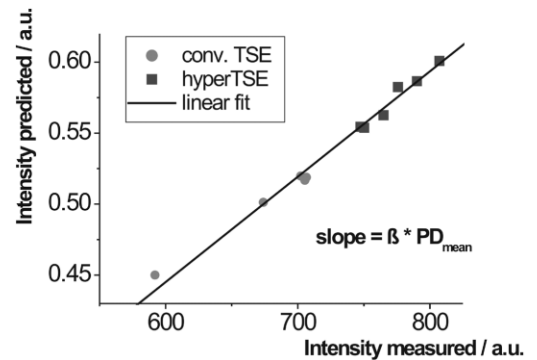

FIG. 2. Measured intensities versus intensity predictions for gray matter of one volunteer (TE = 80 ms, ETL = 25, 3 T). The direct proportional behavior can be observed well (R = 0.99). The slope corresponds to β*PD_{mean}.
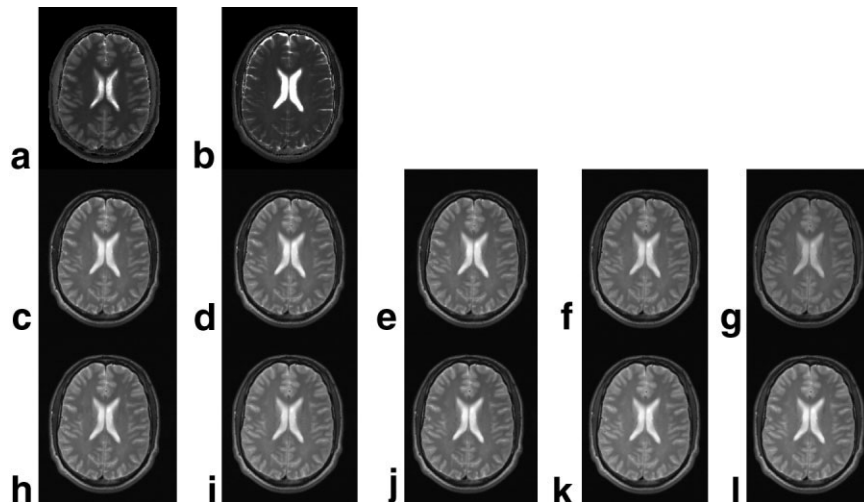
FIG. 3. Images acquired during one series of measurements at 3 T are presented (TE = 80 ms, ETL = 15). In the upper row the T_1 (**a**) and T_2 (**b**) relaxation maps are displayed. For better viewing a window between T_1 = [0;5000] ms and T_2 = [0;500] ms was used. In the middle row the five conventional TSE images (**c–g**) are shown in consecutive order as listed in Table 1. In the lower row five of six TRAPS-TSE (**h–l**) imaging sequences are presented ("TRAPS90_sin1" was omitted). An identical window-leveling (W = 675, L = 1006) was used for all imaging sequences. By comparing the resulting images an SNR decrease and changes in contrast (less T_2 contrast paired with additional T_1 contributions) from the TSE180° (c) to the TSE60° (g) can clearly be identified. Imaging with hyperTSE (h–l) reinstates full signal intensity for all tissues but also exhibits slightly different contrasts compared to the TSE180° due to the unmatched TE_{eff}.

All human studies have been approved by the local ethics review committee and informed written consent was obtained prior to the measurements.

RESULTS

Images acquired during one series of measurements (TE = 80 ms, ETL = 15) at 3 T are shown in Fig. 3 (T_1 map (a), T_2 map (b), conventional (c–g), and TRAPS-TSE (h–l) imaging sequences). By comparing the resulting images an SNR decrease and changes in contrast (less T_2 contrast paired with additional T_1 contributions) from the TSE180° (c) to the TSE60° (g) can clearly be identified. Imaging with hyperTSE (h–l) reinstates full signal intensity for all tissues but also exhibits slightly different contrasts compared to the TSE180° due to the unmatched TE_{eff}.

Table 2 presents the mean relaxation times over all volunteers at 1.5 and 3 T, respectively. As expected, longitudinal relaxation times increase with field strength whereas transverse relaxation times decrease with field strength except for CSF.

As an example, Fig. 2 displays the measured signal intensities versus the predicted relative signal intensities f_{EPG} for gray matter for a single volunteer dataset (TE = 80 ms, ETL = 25, 3 T). The slope of the linear regression

(R = 0.99) corresponds to the tissue specific proton density PD_{mean} multiplied by the additional scaling factor β according to Eq. [1].

The resulting averaged relative proton density values compared to GM are also listed in Table 2.

At 1.5 T, the maximum difference between the measured signal intensities and the theoretically predicted values (Eq [15]) for all tissues and measurements was 2.3%. At 3 T, the corresponding maximum difference was 1.2%.

Figure 4 shows an overview of the measured f_t (Eq. [7]) for CSF, fat, GM, and WM for each sequence (TE = 134 ms, ETL = 15) at 1.5 (a) and 3 T (b). f_t directly represents the true fractional T_2 contribution to the signal. The interindividual standard deviations of the measurements are very low and indeed most of the error bars are virtually invisible, indicating the good reproducibility of the performed measurements and calculations.

As evident from Fig. 4 the T_2 contrast of standard TSE sequences with reduced refocusing flip angles is considerably reduced. For example, TSE sequences with constant flip angles of 120° show a contribution of 87% of T_2 contrast, indicating effective echo time reduction. For the hyperecho / TRAPS implementations, f_t can be as low as ~70% for the sequences, which show the highest reduction in SAR. Figure 4 also demonstrates that the sequence

Table 2
Relaxation Times and Proton Density Ratios of Liquid Proton Pools per Tissue at 1.5 and 3 T

	CSF		Fat		GM		WM	
	1.5 T	3 T	1.5 T	3 T	1.5 T	3 T	1.5 T	3 T
T_1/ms	3916 ± 828	3651 ± 421	561 ± 129	678 ± 149	1213 ± 26	1543 ± 50	679 ± 20	907 ± 27
T_2/ms	1330 ± 619	1429 ± 475	153 ± 30	130 ± 18	126 ± 10	122 ± 8	95 ± 4	92 ± 3
Rel. *PD*	1.09 ± 0.07	1.09 ± 0.05	1.00 ± 0.09	0.91 ± 0.11	1	1	0.87 ± 0.05	0.92 ± 0.04

Note. Mean ± std (interindividual standard deviation) at 1.5 T (n = 10) and 3 T (n = 13).
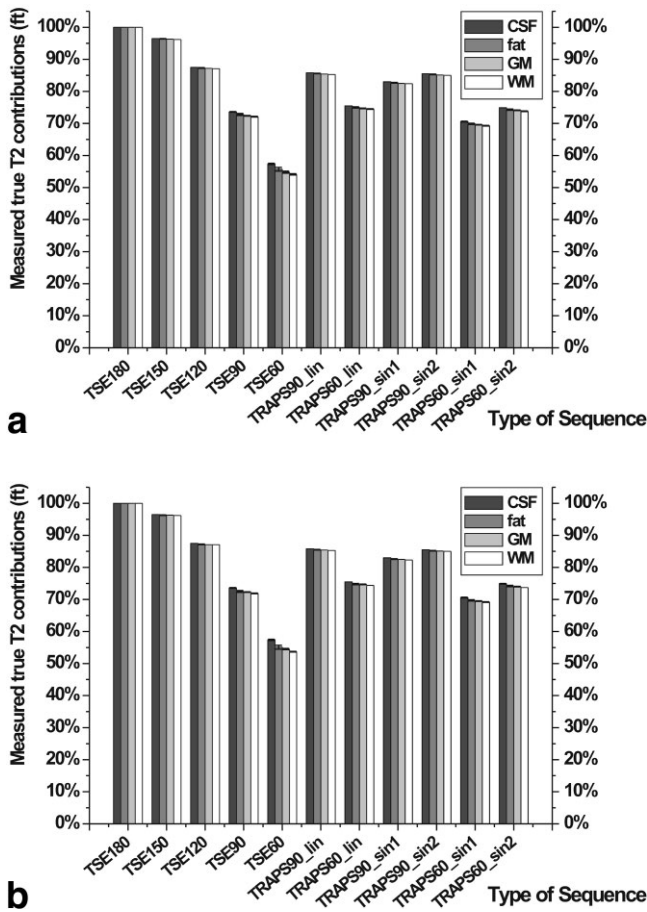
FIG. 4. Measured true T_2 contributions (f_t) for TE = 134 ms, ETL = 15 averaged over all volunteers at 1.5 T (**a**) and 3 T (**b**) are displayed. The error bars are often not visible since the interindividual SD is extremely low. f_t is almost identical for CSF, fat, WM, and GM for one corresponding imaging sequence.

specific effective f_t for each tissue typically differs by less than 1.0% despite pronounced differences in T_1 and T_2. Exceptions are found for conventional TSE90° and TSE60° with higher variations of 1.6 and 3.3%, respectively. A

mean f_t can therefore be defined to characterize the effective T_2 contrast of a given sequence at both field strengths (Tables 3 and 4). Excellent agreement between different f_t is demonstrated by the low standard deviations over all types of tissue.

In addition, Tables 3 and 4 show high correspondence between the measured values of f_t and the a priori estimated T_2 contribution deduced from Eq [10]. For all sequences the predicted T_2 contribution is within 1% of the measured T_2 contributions for all types of tissues. A comparison of the values at 1.5 and 3 T also shows excellent agreement (Fig. 4, Tables 3 and 4).

Conversion of the predicted and experimental f_t values into the effective echo time TE_{eff} according to Eq. [9] indicate that TE corrections can be as high as 30%.

From the known values of f_t appropriate contrast corrections can be directly introduced into the conventional or hyperTSE sequences. Figures 5 and 6 compare images of conventional and hyperTSE sequences with matched TE_{eff}. Figure 5 presents an example of a volunteer with dilated Virchow Robin spaces and another lesion on the left side. Figure 6 was acquired during clinical routine MRI and displays a young patient with a pilocytic astrocytoma. Both hyperTSE images display identical contrast as the conventional TSE180° by using a substantially delayed readout time for the central k-space line.

DISCUSSION

Hyperecho- and TRAPS-TSE (hyperTSE) methods have proven to be useful for T_2 weighted imaging at high fields due to their low SAR (12). In this study it could be shown that the contrast of any TSE sequence with arbitrary flip angles can be predicted by the EPG concept. In addition, the EPG algorithm was employed to introduce a sequence-specific effective echo time TE_{eff} to characterize and control the overall T_2 contrast of TSE sequences with variable refocusing flip angles.

Data Acquisition and Evaluation

Cross-contaminations between adjacent slices and mutual magnetization transfer effects have been carefully avoided

Table 3
Overview of Measured True T_2 Contributions (f_t) Averaged over All Tissues Including Their Mean Estimated T_2 Contribution for TE = 80 ms

Sequence type TE = 80 ms	1.5 T		3 T		1.5 T/3 T estimated f_t/%
	f_t/% ETL = 15	f_t/% ETL = 25	f_t/% ETL = 15	f_t/% ETL = 25	
TSE180°	100.0 ± 0.0	100.0 ± 0.0	100.0 ± 0.0	100.0 ± 0.0	100.0
TSE150°	96.3 ± 0.1	96.3 ± 0.1	96.3 ± 0.1	96.3 ± 0.1	96.2
TSE120°	87.7 ± 0.1	87.7 ± 0.1	87.6 ± 0.1	87.6 ± 0.1	87.5
TSE90°	73.9 ± 0.3	73.9 ± 0.3	73.8 ± 0.4	73.8 ± 0.4	73.4
TSE60°	57.3 ± 0.7	57.3 ± 0.7	57.1 ± 0.8	57.1 ± 0.8	56.1
TRAPS90°_lin	87.0 ± 0.1	87.0 ± 0.1	87.0 ± 0.1	87.0 ± 0.1	86.8
TRAPS60°_lin	77.4 ± 0.2	77.4 ± 0.2	77.3 ± 0.2	77.3 ± 0.2	84.5
TRAPS90°_sin1	84.6 ± 0.1	84.6 ± 0.1	84.6 ± 0.1	84.6 ± 0.1	77.1
TRAPS90°_sin2	87.0 ± 0.1	87.0 ± 0.1	86.9 ± 0.1	86.9 ± 0.1	86.9
TRAPS60°_sin1	73.2 ± 0.3	73.2 ± 0.3	73.1 ± 0.3	73.1 ± 0.3	72.7
TRAPS60°_sin2	77.0 ± 0.2	77.0 ± 0.2	77.0 ± 0.2	77.0 ± 0.2	76.7

Note. Mean ± std of all tissues: CSF, fat, GM, and WM.

Table 4
Overview of Measured True T_2 Contributions (f_t) Averaged over All Tissues Including Their Mean Estimated T_2 Contribution for $TE =$ 134 ms

Sequence type $TE = 134$ ms	1.5 T		3 T		1.5 T/3 T estimated ft/%
	f_t/% $ETL = 15$	f_t/% $ETL = 25$	f_t/% $ETL = 15$	f_t/% $ETL = 25$	
TSE180°	100.0 ± 0.0	100.0 ± 0.0	100.0 ± 0.0	100.0 ± 0.0	100.0
TSE150°	96.4 ± 0.1	96.4 ± 0.1	96.3 ± 0.1	96.3 ± 0.1	96.1
TSE120°	87.2 ± 0.1	87.2 ± 0.1	87.2 ± 0.1	87.2 ± 0.1	87.0
TSE90°	72.7 ± 0.6	72.7 ± 0.6	72.6 ± 0.6	72.6 ± 0.6	71.8
TSE60°	55.5 ± 1.2	55.5 ± 1.2	55.2 ± 1.4	55.2 ± 1.4	53.5
TRAPS90°_lin	85.5 ± 0.2[a]	88.5 ± 0.1[a]	85.5 ± 0.2[a]	88.5 ± 0.1[a]	85.3/88.4[a]
TRAPS60°_lin	74.9 ± 0.4[a]	80.0 ± 0.3[a]	74.8 ± 0.4[a]	80.0 ± 0.3[a]	74.4/79.6[a]
TRAPS90°_sin1	82.6 ± 0.2	82.6 ± 0.2	82.6 ± 0.2	82.6 ± 0.2	82.3
TRAPS90°_sin2	85.2 ± 0.2	85.2 ± 0.2	85.2 ± 0.2	85.2 ± 0.2	85.0
TRAPS60°_sin1	69.9 ± 0.5	69.9 ± 0.4	69.7 ± 0.5	69.7 ± 0.4	69.1
TRAPS60°_sin2	74.3 ± 0.4	74.3 ± 0.5	74.2 ± 0.4	74.2 ± 0.5	73.7

Note. Mean ± std of all tissues: CSF, fat, GM, and WM.
[a]Different ramps were used for $ETL = 15$ and $ETL = 25$ ($TE = 134$ ms); thus, the corresponding T_2 contributions f_t differ (see Table 1).

by using a single slice measurement (19–22). T_1 and T_2 relaxation times were acquired using an identical TSE sequence in order to minimize other and more subtle errors due to eddy current effects and sequence dependent variations in the PSF. For T_1 quantification an additional IR preparation was employed. Identical TSE sequences for T_1 and T_2 assessment as well as imaging were used in order to allow pixel-by-pixel comparisons between images.

The acquisition time for the whole experimental protocol was restricted to approximately 60 min in order to ensure compliance of the volunteers and to enhance the reliability of the data.

Relaxation Times and Proton Densities

A rather broad range of T_1 and T_2 values for brain tissue has been reported in the literature, probably due to different measurement techniques and—to a minor degree—to varying anatomic locations used in the evaluation. Literature values for T_1 at 1.5 T range between 633 and 728 ms for white matter and between 998 and 1304 ms for cortical gray matter (23–26). Our values presented in Table 2 agree very well with these reports. $T_{1,WM}$ also shows excellent agreement with the predicted value of $T_{1,WM\_1.5T} = 652$ ms according to the theoretical considerations by Fi-

scher et al. ("two step high field relaxation dispersion for WM" (27)).

So far there have not been many published data on longitudinal relaxation times at 3 T. First reports (28,29) state T_1 values between 832 and 1110 ms for white matter and between 1150 and 1470 ms for cortical gray matter, depending on the location in the brain. The values reported in Table 2 agree very well with both reports for white matter and closely match the upper range of gray matter. Considering published results for T_1 at 4 T (30) both $T_{1,WM}$ and $T_{1,GM}$ are within in the expected range of longitudinal relaxation times at 3 T. T_{1,WM_3T} also shows excellent agreement with the empiric predictions ($T_{1,WM\_3T} = 880$ ms) from (27) (see above). However, no significant B_0 dependence of $T_{1,CSF}$ has been observed between 1.5 and 3 T, which may be expected from longitudinal relaxation theory since CSF is much more similar to water than tissue. Our experimental value may indicate that the measured T_1 is not the true T_1 but shortened by motional effects although Clare and Jezzard report an almost identical value for T_{1,CSF_3T} (31). This assumption is supported by the higher SD of CSF values compared to GM and WM at 1.5 as well as 3 T.

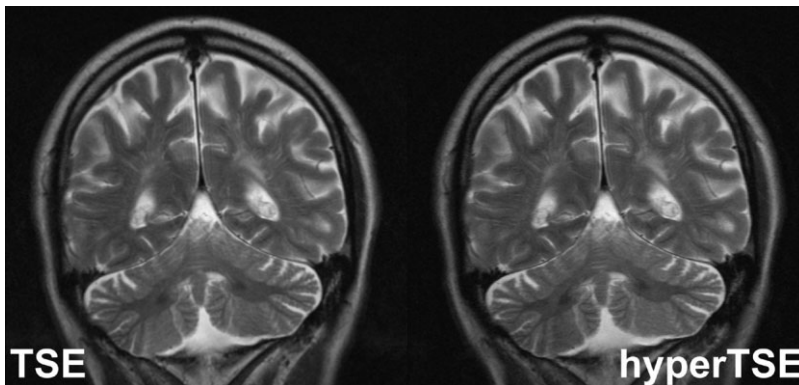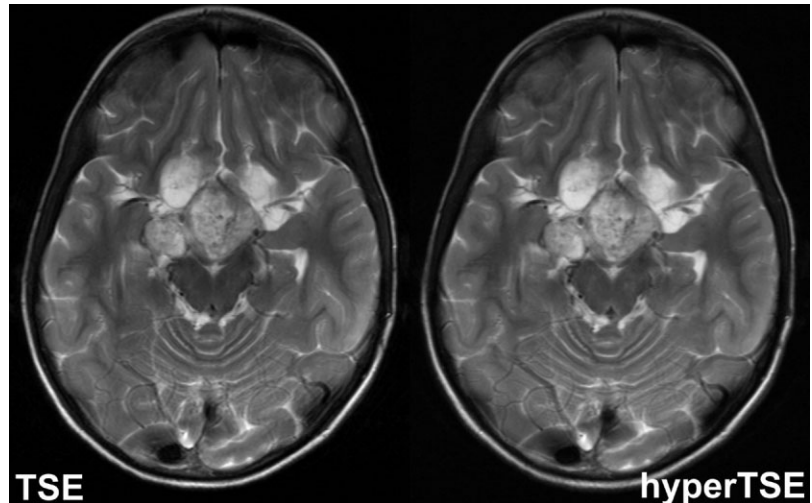The mentioned empiric model for longitudinal relaxation dispersion can also be employed for predictions of

FIG. 5. Comparison of a TSE and hyperTSE image at 3 T from a volunteer with later diagnosed dilated Virchow Robin spaces and another lesion on the left side. An intrinsic T_2 weighted contrast correction with the validated EPG concept was employed. Both display the same contrast and high resolution.

FIG. 6. Comparison of a TSE and hyperTSE image at 3 T from a pediatric patient with a pilocytic astrocytoma. The images with matched TE_{eff} were acquired during clinical routine MRI. Both images resolve the pathology equally well.

T_1 of gray matter. Estimated T_1 relaxation times using a "one step high field relaxation dispersion for GM" are close to the lower range of reported values in the literature and also differ from our results. Considering that the corresponding predictions for $T_{1,GM}$ at even higher field strengths such as 4 T (30) do not coincide with this theory as well, an adjustment of the model for predictions of gray matter relaxation times at high fields may be necessary.

Transverse relaxation may best be characterized with a multiexponential decay (32,33). For a monoexponential model, T_2 values at 1.5 T are usually in the range between 66 and 80 ms for white matter as well as 80 and 100 ms for cortical gray matter (23–25,30,32,34,35). Our measured values (Table 2) are somewhat higher compared to most published data. Possible explanations of these discrepancies include increased partial volume effects from CSF. However, this assumption is unlikely since the effect would be expected to vary between subjects and, thus, lead to an increased SD of the average values. In addition, the use of slice selective refocusing pulses that lead to a variation of flip angles across the slice profile (21,33,36,37) or B_1 inhomogeneities that have a higher impact on slice selective pulses than on nonselective RF pulses as shown in (33,36) may result in a nonperfect refocusing behavior, thereby prolonging the measured T_2 decay. An additional factor may be the use of a rather short echo spacing ESP = 8 ms, which diminishes diffusion effects leading to a shorter T_2' (38).

A previous study of the transverse relaxation times at 3 T reports $T_2 = 80$ ms for white matter and a range of T_2 between 99 and 117 ms for gray matter depending on the sex of the volunteers (29). The latter difference between males and females was significant ($P < 0.0001$). Our values (Table 2) are somewhat higher but still in a similar range. Especially our gray matter value of T_2 is close to the "male $T_{2,GM}$" assessed by Wansapura et al. (29). In our study we did not find a significant difference between males and females, which may be due to the small number of female subjects ($n = 2$).

The T_2 values for gray and white matter exhibit a non-significant trend to lower values for higher field strength B_0, potentially related to increased T_2' effects in local susceptibility fields, which increase with field strength. The reduction of T_2 of fat is more pronounced most probably as a consequence of *J*-coupling dependent dephasing, which increases with the chemical shift difference and, thus, with field strength.

PD ratios for the "visible" liquid proton pool (Table 2) are in good agreement with previously published values at 1.5 T, which have been reported to be within 0.83 and 0.86 for PD_{WM}/PD_{GM} (25,32,35,39) and between 1.02 and 1.25 for PD_{CSF}/PD_{GM} (25,40).

Flip-Angle-Dependent Signal Variations

It could be shown that the extended phase graph concept can accurately predict the signal intensities of any tissue in generic TSE sequences at 1.5 and 3 T. Although all calculations were performed via a hard pulse approximation neglecting influences such as slice profiles and B_1 variations, excellent agreement within 2% or better between predicted and measured results was observed. These results further illustrate the usefulness of the EPG concept for calculating refocusing flip angles for predefined signal amplitudes (17).

T_1 and T_2 Contributions and Estimation of Effective Echo Time TE_{eff}

Our results demonstrate that a single f_t value, independent of T_1 and T_2, can be used to characterize the effective T_2 contrast of any TSE sequence with arbitrary flip angles (Fig. 4, Tables 3 and 4). Therefore, an explicit TE_{eff} can be determined and used to characterize the T_2 contrast of such sequences, which was previously demonstrated by simulations for TRAPS (8,17) and is now experimentally validated in vivo.

It should be noted that even for constant flip angle sequences the effects of stimulated echo contributions is quite pronounced. In the TSE120° sequence f_t is 87% leading to 13% T_1 contribution to the signal intensity. As a result, reduced T_2 contrast must be taken into account when using low flip angle TSE in clinical routine protocols like breathhold abdomen imaging at 3 T. For sequences

employing even lower flip angles—and thus more pronounced SAR reduction—TE_{eff} can be reduced by up to 30% compared to the nominal readout time of the k-space center. Thus, appropriate adaptations have to be made to ensure identical T_2 contrast.

No significant differences have been observed between sequences at identical echo times but different echo train lengths, which further emphasizes the validity of the concept that the contrast behavior is determined by the signal at the center of k-space.

Adaption of T_2 Contrast and TE

The fact that f_t is largely independent of T_1 and T_2 and, thus, can be calculated a priori based on the known flip angles alone is of great practical value. It allows one to automatically match the effective TE_{eff} to yield the T_2 contrast expected from using a conventional TSE sequence with ideal 180° RF pulses. In our implementation the echo readout time is automatically adapted to generate constant and identical T_2 contrast irrespective of the type of flip angle variation used to save SAR. Although shifting of the readout time, i.e., TE, of course works only in increments of the echo spacing, the resulting mismatch in TE_{eff} between conventional TSE and hyperTSE is, however, negligible in practice.

The robustness of f_t to various T_1 and T_2 combinations was illustrated by comparisons between high-resolution T_2 weighted conventional TSE180° and hyperTSE with prolonged TE to match the desired TE_{eff}.

Prolongation of the signal decay and shift of TE to later echoes is actually an advantage since it enables the use of longer echo trains and thus to reduce the overall acquisition time. Longer echo trains also provide more flexibility with respect to flip angle variations and thus SAR savings. It should be kept in mind, however, that for tissues with short T_2 and short T_1 the use of a prolonged TE may lead to reduced signal intensity.

The calculation of an adapted TE_{eff} is based on the approximation $T_1 \gg T_2$. This assumption is not strictly valid for CSF where $T_{2,CSF}$ is on the same order of magnitude as $T_{1,CSF}$. However, as shown by the tissue-dependent f_t values in Fig. 4 and Tables 3 and 4, this approximation still works very well for CSF.

Although it was not the focus of this study, it should be noted that no loss in image resolution was observed for the hyperTSE sequences. Consequently, prudent use of flip angle variations preserves or may even improve the point spread function of TSE in accordance with our previous reports (8,17), whereas blurring has been demonstrated to occur using other than optimized flip angle variation schemes (10).

CONCLUSIONS

Extended phase graph concepts can be used to accurately predict the intensity of tissues of a given TSE sequence with arbitrary flip variations. A single parameter f_t accurately describes the effective T_2 contrast of a given sequence irrespective of the tissue type. Thus, an effective echo time TE_{eff} can be used to predict the T_2 contrast of any such sequence. TE_{eff} can be calculated by employing the EPG concept and is demonstrated to be independent of the field strength and the observed tissue type. Sequences using low flip angles used to reduce SAR by 70% and more show significantly different T_2 contrast at identical echo times. Using the recalculated effective echo time TE_{eff}, identical T_2 contrast is reestablished and imaging can be performed at drastically reduced SAR.

REFERENCES

1. Hennig J, Nauerth A, Friedburg H. RARE imaging: a fast imaging method for clinical MR. Magn Reson Med 1986;3:823–833.
2. Thomas DL, De Vita E, Roberts S, Turner R, Yousry TA, Ordidge RJ. High-resolution fast spin echo imaging of the human brain at 4.7 T: implementation and sequence characteristics. Magn Reson Med 2004; 51:1254–1264.
3. Griswold MA, Jakob PM, Heidemann RM, Nittka M, Jellus V, Wang J, Kiefer B, Haase A. Generalized autocalibrating partially parallel acquisitions (GRAPPA). Magn Reson Med 2002;47:1202–1210.
4. Pruessmann KP, Weiger M, Scheidegger MB, Boesiger P. SENSE: sensitivity encoding for fast MRI. Magn Reson Med 1999;42:952–962.
5. Hennig J, Wieben O, Weigel M. Signal-to-noise in TSE-imaging with incomplete k-space coverage: strategies and implications for low-SAR imaging at high fields. In: Proceedings of the 12th Annual Meeting of ISMRM, Kyoto, Japan, 2004. p 2142.
6. Feinberg DA, Hale JD, Watts JC, Kaufman L, Mark A. Halving MR imaging time by conjugation: demonstration at 3.5 kG. Radiology 1986; 161:527–531.
7. Hennig J. Multiecho imaging sequences with low refocusing flip angles. J Magn Reson 1988;78:397–407.
8. Hennig J, Weigel M, Scheffler K. Multiecho sequences with variable refocusing flip angles: optimization of signal behavior using smooth transitions between pseudo steady states (TRAPS). Magn Reson Med 2003;49:527–535.
9. Hennig J, Scheffler K. Hyperechoes Magn Reson Med 2001;46:6–12.
10. Busse RF. Reduced RF power without blurring: correcting for modulation of refocusing flip angle in FSE sequences. Magn Reson Med 2004; 51:1031–1037.
11. Mugler JP, Wald LL, Brookeman JR. T2-weighted 3D spin-echo train imaging of the brain at 3 Tesla: reduced power deposition using low flip-angle refocusing RF pulses. In: Proceedings of the 9th Annual Meeting of ISMRM, Glasgow, Scotland, 2001. p 438.
12. Weigel M, Ziyeh S, Mader I, Weber J, Hennig J. Neuroradiological Applications of Hyperecho-TSE sequences at 3T: first clinical results. In: Proceedings of the 12th Annual Meeting of ISMRM, Kyoto, Japan, 2004. p 76.
13. Weigel M, Hennig J Low SAR inversion recovery weighted TSE sequences using TRAPS: parameter optimization and examples. In: Proceedings of the 12th Annual Meeting of ISMRM, Kyoto, Japan, 2004. p 694.
14. Alsop DC. The sensitivity of low flip angle RARE imaging. Magn Reson Med 1997;37:176–184.
15. Le Roux P, Hinks RS. Stabilization of echo amplitudes in FSE sequences. Magn Reson Med 1993;30:183–190.
16. Hennig J, Scheffler K. Easy improvement of signal-to-noise in RARE-sequences with low refocusing flip angles. Magn Reson Med 2000;44: 983–985.
17. Hennig J, Weigel M, Scheffler K. Calculation of flip angles for echo trains with predefined amplitudes with the extended phase graph (EPG)-algorithm: principles and applications to hyperecho and TRAPS sequences. Magn Reson Med 2004;51:68–80.
18. Hennig J. Echoes—how to generate, recognize, use or avoid them in MR-imaging sequences. Conc Magn Reson 1991;3:125–143.
19. Melki PS, Mulkern RV. Magnetization transfer effects in multislice RARE sequences. Magn Reson Med 1992;24:189–195.
20. Santyr GE. Magnetization transfer effects in multislice MR imaging. Magn Reson Imaging 1993;11:521–532.

21. Crawley AP, Henkelman RM. Errors in T2 estimation using multislice multiple-echo imaging. Magn Reson Med 1987;4:34−47.

22. Kucharczyk W, Crawley AP, Kelly WM, Henkelman RM. Effect of multislice interference on image contrast in T2- and T1-weighted MR images. Am J Neuroradiol 1988;9:443−451.

23. Breger RK, Rimm AA, Fischer ME, Papke RA, Haughton VM. T1 and T2 measurements on a 1.5-T commercial MR imager. Radiology 1989;171: 273−276.

24. Vymazal J, Righini A, Brooks RA, Canesi M, Mariani C, Leonardi M, Pezzoli G. T1 and T2 in the brain of healthy subjects, patients with Parkinson disease, and patients with multiple system atrophy: relation to iron content. Radiology 1999;211:489−495.

25. Schmitt P, Griswold MA, Jakob PM, Kotas M, Gulani V, Flentje M, Haase A. Inversion recovery TrueFISP: quantification of T(1), T(2), and spin density. Magn Reson Med 2004;51:661−667.

26. Henderson E, McKinnon G, Lee TY, Rutt BK. A fast 3D look-locker method for volumetric T1 mapping. Magn Reson Imaging 1999;17: 1163−1171.

27. Fischer HW, Rinck PA, Van Haverbeke Y, Muller RN. Nuclear relaxation of human brain gray and white matter: analysis of field dependence and implications for MRI. Magn Reson Med 1990;16:317−334.

28. Ethofer T, Mader I, Seeger U, Helms G, Erb M, Grodd W, Ludolph A, Klose U. Comparison of longitudinal metabolite relaxation times in different regions of the human brain at 1.5 and 3 Tesla. Magn Reson Med 2003;50:1296−1301.

29. Wansapura JP, Holland SK, Dunn RS, Ball WS, Jr. NMR relaxation times in the human brain at 3.0 tesla. J Magn Reson Imaging 1999;9: 531−538.

30. Jezzard P, Duewell S, Balaban RS. MR relaxation times in human brain: measurement at 4 T. Radiology 1996;199:773−779.

31. Clare S, Jezzard P. Rapid T(1) mapping using multislice echo planar imaging. Magn Reson Med 2001;45:630−634.

32. Brix G, Schad LR, Lorenz WJ. Evaluation of proton density by magnetic resonance imaging: phantom experiments and analysis of multiple component proton transverse relaxation. Phys Med Biol 1990;35:53−66.

33. Poon CS, Henkelman RM. Practical T2 quantitation for clinical applications. J Magn Reson Imaging 1992;2:541−553.

34. Deoni SC, Peters TM, Rutt BK. High-resolution T1 and T2 mapping of the brain in a clinically acceptable time with DESPOT1 and DESPOT2. Magn Reson Med 2005;53:237−241.

35. Whittall KP, MacKay AL, Graeb DA, Nugent RA, Li DK, Paty DW. In vivo measurement of T2 distributions and water contents in normal human brain. Magn Reson Med 1997;37:34−43.

36. Sled JG, Pike GB. Correction for B(1) and B(0) variations in quantitative T(2) measurements using MRI. Magn Reson Med 2000;43:589−593.

37. Majumdar S, Orphanoudakis SC, Gmitro A, O'Donnell M, Gore JC. Errors in the measurements of T2 using multiple-echo MRI techniques. I. Effects of radiofrequency pulse imperfections Magn Reson Med 1986; 3:397−417.

38. Michaeli S, Garwood M, Zhu XH, DelaBarre L, Andersen P, Adriany G, Merkle H, Ugurbil K, Chen W. Proton T2 relaxation study of water, N-acetylaspartate, and creatine in human brain using Hahn and Carr−Purcell spin echoes at 4T and 7T. Magn Reson Med 2002;47:629−633.

39. Roberts DA, Rizi R, Lenkinski RE, Leigh JS, Jr. Magnetic resonance imaging of the brain: blood partition coefficient for water: application to spin-tagging measurement of perfusion. J Magn Reson Imaging 1996; 6:363−366.

40. Haacke EM, Brown RW, Thompson MR, Venkatesan R. In: Magnetic resonance imaging—physical principles and sequence design. 1st ed. New York: Wiley-Liss; 1999. p 457.